DOI: 10.1111/cgf.12911
Eurographics Conference on Visualization (EuroVis) 2016
K.-L. Ma, G. Santucci, and J. van Wijk
(Guest Editors)

Volume 35 (2016), Number 3

Semi-automatic Vortex Flow Classification in 4D PC-MRI Data of the Aorta

M.Meuschke[1], B. Köhler[1], U. Preim[2], B. Preim[1], K. Lawonn[3]

[1]Department of Simulation and Graphics, University of Magdeburg, Germany
[2]Department of Diagnostic Radiology, Municipal Hospital, Magdeburg, Germany
[3]Institute of Computational Visualistics, University of Koblenz - Landau, Germany

Abstract

We present an Aortic Vortex Classification (AVOCLA) that allows to classify vortices in the human aorta semi-automatically. Current medical studies assume a strong relation between cardiovascular diseases and blood flow patterns such as vortices. Such vortices are extracted and manually classified according to specific, unstandardized properties. We employ an agglomerative hierarchical clustering to group vortex-representing path lines as basis for the subsequent classification. Classes are based on the vortex' size, orientation and shape, its temporal occurrence relative to the cardiac cycle as well as its spatial position relative to the vessel course. The classification results are presented by a 2D and 3D visualization technique. To confirm the usefulness of both approaches, we report on the results of a user study. Moreover, AVOCLA was applied to 15 datasets of healthy volunteers and patients with different cardiovascular diseases. The results of the semi-automatic classification were qualitatively compared to a manually generated ground truth of two domain experts considering the vortex number and five specific properties.

Categories and Subject Descriptors (according to ACM CCS): I.4.9 [Computer Graphics]: Image Processing and Computer Vision—Applications

1. Introduction

Cardiovascular diseases (CVDs) represent the world's leading cause of death. Medical researchers are interested in better understanding the causes of their initiation and evolution that depends strongly on the blood flow characteristics. Therefore, information about the patient-specific hemodynamics are used that can be non-invasively acquired by four-dimensional phase-contrast magnetic resonance imaging (4D PC-MRI) [DBB*15].

A qualitative data analysis enables the visualization of vortices that are considered as an indicator of pathologies [HHM*10, HWS*12, MBS*15]. To investigate the influence of vortices on CVDs, medical studies with homogeneous patient groups are performed. The vortex occurrences are counted and classified according to specific characteristics in a binary manner. Such a vortex analysis is manually performed with common flow visualization techniques such as particle animations. This is a time-consuming, subjective and error-prone process with a high inter-observer variability. Moreover, the binary classifications are often not sufficient to describe the vortex behavior, but a more detailed visual assessment is challenging. However, to uncover correlations between vortex flow and certain CVDs, the classification results of different datasets should be comparable. This requires an objective classification according to clearly defined criteria.

In this work, we present a method for a semi-automatic classification of aortic vortices. Vortex-representing path lines were extracted from 4D PC-MRI data using the line predicates technique by Köhler et al. [KGP*13]. An agglomerative hierarchical clustering is applied to determine vortex entities. The vortex properties are calculated semi-automatically, which leads to an objective vortex description and decreasing inter-observer variability. We introduce a 2D and 3D visualization to analyze the classification results, see Fig. 1. In a qualitative evaluation, we compared the results of our approach with manually classified vortices of two domain experts. For this, we used two healthy and 13 pathological 4D PC-MRI datasets. Moreover, we performed a user study to evaluate if the 2D and 3D visualization are able to convey the classification results. In summary, we make the following contributions:

- A list of classification criteria from medical studies that deal with the classification of aortic vortices.
- A semi-automatic vortex classification, which is qualitatively compared to a ground truth of two domain experts.
- The classification results extend the binary classifications.
- A 2D and 3D visualization of the classification results is presented that are evaluated in a user study.

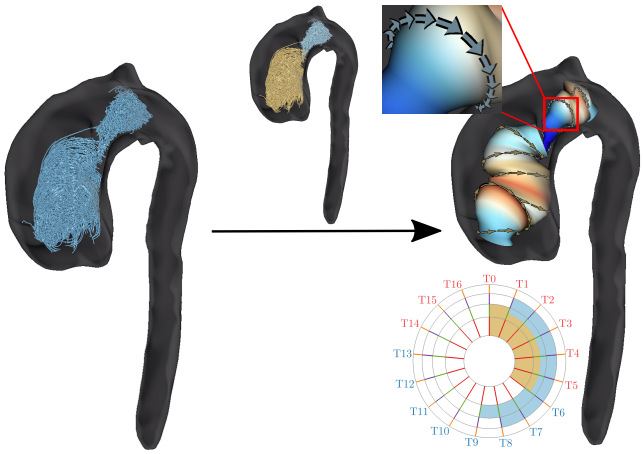

Figure 1: *AVOCLA is applied to a patient dataset with an aortic dilation. Starting from the path lines, two clusters are generated that are visualized by a 2D plot and a 3D glyph.*

2. Related Work

Visualization and Exploration of Blood Flow. 4D PC-MRI are highly complex flow data whose visualization is often affected by visual clutter and occlusions. Van Pelt et al. [vPBB*10] presented illustrative renderings to depict time-dependent blood flow dynamics. Gasteiger et al. [GNKP10] presented a ghosted view approach, which allows a simultaneous depiction of the vessel morphology and blood flow. Lawonn et al. [LGP14] provided a vessel visualization technique such that the vessel morphology can be better perceived and the flow information is always visible.

These methods cannot assist the user to interpret the blood flow concerning specific flow patterns such as vortices or high-velocity jets. To simplify the vector field analysis and to answer specific questions, several methods for extraction and visualization of such features are presented. Born et al. [BPM*13] used the *line predicate* approach introduced by Salzbrunn et al. [SS06] to extract interesting flow characteristics including *inflow jets* and blood with high residence times in the aorta. Gasteiger et al. [GLvP*12] applied line predicates to simulated blood flow data of cerebral aneurysms to determine inflow jets and *impingement zones*. Köhler et al. [KGP*13] determined the λ_2-criterion as most suitable to filter path lines that represent vortex regions. Furthermore, Köhler et al. [KMP*15] projected the vortex-representing path lines to a 2D plot that shows present vortex flow in the aorta at one glance. Oeltze et al. [OLK*14] compared different state-of-the-art clustering techniques to cluster 3D streamlines in cerebral aneurysms and determined cluster representatives that display major flow directions. Van Pelt et al. [vPJtHRV12] applied a hierarchical clustering method to the phase images of aortic 4D PC-MRI data to achieve a more abstract flow depiction. Each cluster is visualized by a representative path arrow. Born et al. [BMGS13] used illustrative visualizations to depict steady flow features extracted from 4D PC-MRI data based on line predicates. An overview of the visualization of simulated and measured flow data can be found in the summaries by Preim and Botha [PB13], Vilanova et al. [VPvP*14] and Köhler et al. [KBV*16].

Classification of Aortic Vortices. Recent medical studies [HHM*10, HWS*12, FMH*11] evaluate the number of occurring vortices in patient datasets and classify them manually according to the following characteristics:

- The *shape* refers to the extent of a vortex. Rather compressed vortices are called vortex, elongated structures on the other hand are called helix.
- The *time of occurrence* in the cardiac cycle is differentiated according to systole and/or diastole.
- The *vessel section* locates a flow pattern to belong to the ascending aorta, aortic arch and descending aorta.
- The *size* is divided into minor and pronounced, depending on the occupation of the vessel diameter by the vortex.
- The *rotation direction* (RD) is divided into right- and left-handed with the centerline as a reference.

To facilitate the vortex analysis, computer-based classification methods were introduced. Von Spiczak et al. [vSCG*15] introduced a vortex classification using the vorticity and a vortex core detection method. However, the approach is sensitive to noise, which reduces the result quality. Other works identify and classify vortex flow based on pattern matching [HEWK03, vPFCV14]. A major disadvantage of these methods is that the number of distinguishable patterns depends on the number of used template flow patterns. Therefore, we calculate the vortex characteristics based on geometrical properties and relations of the representing path lines and the vessel surface.

3. Medical Background

Blood is being pumped in a complex cycle of vessels by the heart contraction, with the aorta as the largest artery. Their caliber dimensions of about 2-3 cm allow the acquisition of an easily measurable signal for a meaningful blood flow analysis. During systole, oxygenated blood from the left ventricle passes the aortic valve (AV) into the ascending aorta and is then supplied to the body, see Fig. 2. Deoxygenated blood is pumped from the right ventricle through the pulmonary valve into the pulmonary artery. During diastole, the AV is closed to prevent blood back flow.

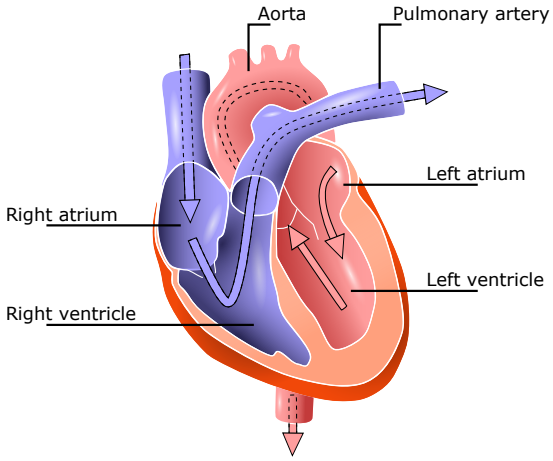

Figure 2: *Structure of the human heart.*

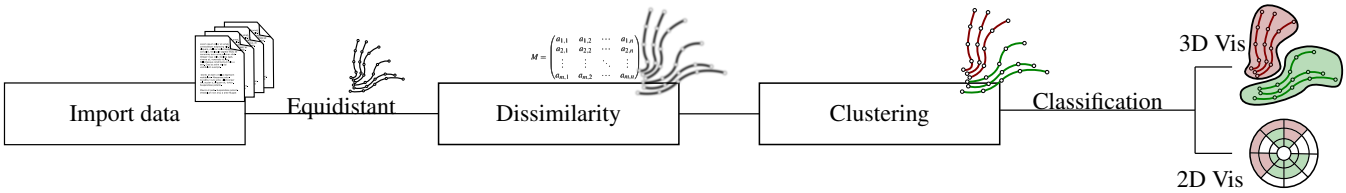

Figure 3: *The pipeline of AVOCLA. The imported data contains the surface mesh, the centerline and the vortex-representing path lines. The path lines and the centerline are sampled equidistantly and a dissimilarity matrix is calculated as input for the clustering. Each clustered vortex is classified and depicted by a 2D and 3D visualization.*

3.1. Selected Pathologies and Related Flow Behavior

Healthy persons exhibit only a slight systolic helix in the aortic arch, which is considered as physiological [KYM*93]. CVDs lead to altered vessel geometries that increase the probability of emerging vortex flow patterns. In aortic aneurysms large helical vortices are detected and additional helices and vortices in the ascending aorta that are not occurring in healthy subjects [HMW*07, FHJ*07]. Frydrychowicz et al. [FMH*11] investigated blood flow in healthy persons and patients with an aortic coarctation that show additional helix or vortex formations. François et al. [FSS*12] examined flow patterns in patients with a tetralogy of Fallot and found increased helical or vortical flow in the right ventricle as well as the pulmonary artery compared to healthy volunteers. Patients with a bicuspid AV show strong correlations to helical flow in the ascending aorta during systole [HHM*10, MBS*15]. The vortex RD was depending on which of the three leaflets are fused [MBS*15]. Patients with Marfan Syndrome showed increased helical and vortical flow in the ascending and descending aorta compared to healthy subjects [MGH*11, GMH*12]. Moreover, an increased susceptibility to ectasia development was observed in such patients, which probably results from the complex flow patterns.

3.2. Data Acquisition and Preprocessing

A 4D PC-MRI dataset contains each three (x-, y- and z-direction) time-resolved phase and magnitude images that describe the flow direction and strength, respectively. All temporal positions together represent one full heart beat. A 3 T Siemens Magnetom Verio MR scanner was used with a maximum expected velocity (V_{ENC}) of 1.5 m/s per dimension. The spatio-temporal resolution is 1.77 $\times$ 1.77 $\times$ 3.5 mm^3 \ 50 ms with a 132 $\times$ 192 grid for each of the 15 to 23 slices and 14 to 21 time steps. Phase wraps and velocity offsets are corrected and a temporal maximum intensity projection (TMIP) is generated from the magnitude images as basis for a binary segmentation [KGP*13]. The vessel surface is extracted via Marching Cubes and then used to extract the centerline [PVS*09] that is presented as a sequence of equidistant (0.5 mm) points. Vortex-representing path lines are extracted using the line predicates technique [KGP*13].

4. Requirement Analysis

Our approach is based on the discussion with two domain experts: a radiologist specialized in cardiac imaging with four years of work experience and an expert specialized in the visualization of 4D PC-MRI data with three years of work experience. Both are co-authors of this paper. The classification of vortices requires a reliable path line clustering that does not need a priori selection of the cluster number, because the number of vortices is unknown. Moreover, the clustering should be able to group spatio-temporally adjacent vortices even if laminar flow and noise is existent. Both clustering and classification are required to be performed automatically. However, due to the enormous anatomic diversity, the automatically calculated results will not always be correct. Thus, the experts should be able to manually correct the results. The calculated vortex properties should reflect and extend the binary expert classifications according to minor and pronounced flow or helix and vortex. Besides a tabular representation, the experts want an adequate visualization of the classification results in order to verify and interpret them better. They commented that an occlusion-free depiction of the spatio-temporal vortex behavior would be very helpful. Therefore, we need a visualization that improves the exploration of the vortex properties. We summarize the main requirements for the semi-automatic vortex classification:

Req. 1. Clustering. The clustering should be robust towards noise and able to separate spatio-temporal vortices without the need of a cluster number as input.

Req. 2. Contribution of expert knowledge. Although the clustering and classification of vortices is performed automatically, the experts should be able to correct the results.

Req. 3. Classification criteria. The classification results represent the most binary vortex classification by the physicians and should be extendable.

Req. 4. Vortex visualization. A vortex visualization is needed that depicts the vortex characteristics helpfully.

5. Semi-automatic Vortex Classification

In this section, we describe our pipeline to classify aortic vortices semi-automatically (see Fig. 3). The imported data contains the surface mesh, the vortex path lines, and the centerline. Here, the path lines and the centerline are equally sampled. Then, pairwise path line dissimilarity values are calculated and stored in a matrix. Based on this dissimilarity matrix, the clustering generates a grouping of the path lines. Each clustered vortex is classified according to predefined properties. Finally, the classification results are visualized

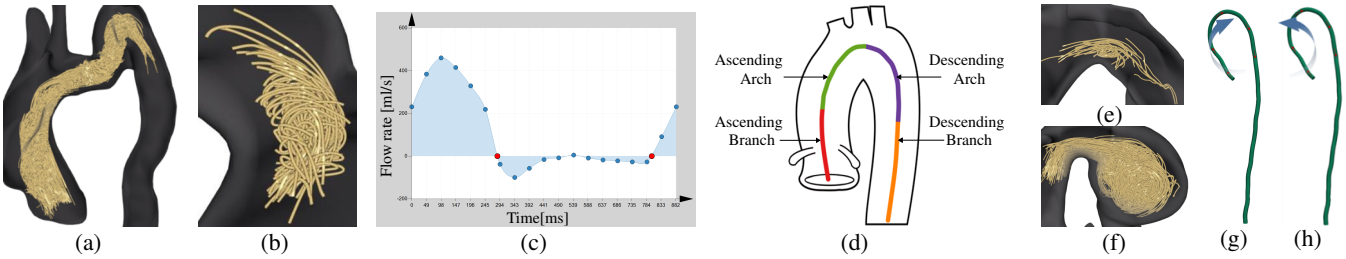

Figure 4: *Vortex classification criteria. The shape is divided into helix (a) and vortex (b). The flow curve (c) is used to determine the temporal behavior. For the spatial classification, four aortic sections (d) are distinguished. The size is divided into minor (e) and pronounced (f) flow and the RD is distinguished into right- (g) and left-handed (h).*

using a 2D plot depiction and a 3D glyph-based representation. In the following, we explain the pipeline in detail.

5.1. Clustering of Aortic Vortex Flow

The vortex classification requires a precise definition of spatio-temporal vortex entities. For this purpose, we used our previous work for vortex clustering represented by path lines [MLK*16]. In this work, we combined a reliable dissimilarity measure with three clustering methods that do not need a priori selection of the cluster number. The clustering results were qualitatively compared to a manually generated ground truth of two domain experts. Our measure calculates pairwise path line dissimilarities using Euclidean and temporal distances. Moreover, we consider the difference between two lines according to the averaged centerline distance. This enables a reliable grouping of spatio-temporally adjacent vortices. The resulting distance values between two given path lines are accumulated and stored in a squared symmetric dissimilarity matrix $\mathbf{M}$ as basis for the clustering. The entry $\mathbf{M}_{ij}$ corresponds to the dissimilarity between path lines i and j with $\mathbf{M}_{ii} = 0$. We compared an agglomerative hierarchical, a density-based and a spectral clustering technique. The first approach has been determined to produce the most reliable results, wherefore we used it for the vortex clustering. For further details we refer to Meuschke et al. [MLK*16].

5.2. Classification of Clustered Vortices

We developed a semi-automatic vortex classification according to five properties introduced in Sec. 2. In this section, we describe the implementation of the classification in detail.

Vortex Shape. In manual classifications, the vortex shape is divided into helix (Fig. 4(a)) and vortex (Fig. 4(b)) depending on which shape is more present in the vortex. This binary classification is not always appropriate because in most cases vortices take on an intermediate shape of both. Therefore, we make the assessment of intermediate shapes more objective, as we calculate the percentage of helical and vortical flow (related to Req. 3). Depending on the strength of the line predicate-based filtering, laminar flow may occur that we distinguish as third shape.

We determine for each path line the covariance matrix of the spatial path line point positions and the corresponding eigenvalues. Depending on the eigenvalues, one of the three shapes is assigned to each path line. We assume that a perfect vortical, helical or laminar line is represented by a circle (λ_1=λ_2, λ_3=0), a helix (λ_1 is dominant, λ_2=λ_3) and a line ($\lambda_1 \neq 0$, λ_2=λ_3=0), respectively, where $\lambda_1, \lambda_2, \lambda_3$ are the ordered eigenvalue absolutes. Usually, path lines take on a shape between perfect circle and helix or between helix and a line. These intermediate shapes can be described by a compression or stretching of a perfect helix that is represented by the following formulation:

$$\vec{v}(t) = \begin{pmatrix} r \cdot cos(2\pi t) \\ r \cdot sin(2\pi t) \\ h \cdot t \end{pmatrix} \quad (1)$$

The parameter t represents the number of helix turns, r is the radius, and h describes the helix stretching. Fig. 5 shows seven helices with varying h. In the following, we assume that the height stays constant. By increasing h (red to blue helix), the turns of the helix are reduced until almost a straight line is produced. Changing h causes a modification in the corresponding eigenvalues, see the graph in Fig. 5. A parabolic curve represents the behavior of the eigenvalues depending on h. The eigenvalues of the color dots correlate to the colored helices. Based on the parabola, we are able to determine a shape for each path line. Therefore, we divide the curve into three sections separating the points into vortical flow (first red point to third beige point), helical flow (third beige point to last cyan point) and laminar flow (behind last cyan point). Depending on the eigenvalues of a path line, AVOCLA identifies the nearest point on the parabola, which gives us the corresponding section of the curve. The separation points (third beige and last cyan point) were determined empirically so that AVOCLA correctly identifies vortices that are clearly classified as helix or vortex in the ground truth.

Based on the mere eigenvalue analysis, lines that run initially vortically and then laminar may be classified as helical, whereas from a medical perspective the vortical behavior is far more interesting. To correct possible wrong classifications, we determine the torsion for all points of helical lines, which is high for helical lines that are sharply twisting out of a plane. Lines that are incorrectly classified as helical are corrected according to their low torsion.

This requires the introduction of a torsion threshold τ_v, with the torsion τ of Eq. 1 given by $\tau = \frac{h}{(r^2+h^2)}, r = 1$. For $h \leq 1$ the torsion increases, which corresponds to the transition from a circle in the plane (vortex: τ=0) into a helix in space with maximum torsion ($\tau = \tau_{max} = 1/(2 \cdot r)$). For $h > 1$ the torsion decreases, which corresponds to the extension of a helix to a straight line. The threshold τ_v is described as $\tau_{max} \cdot c$ with r being set to the average vessel radius. Often, helical and vortical lines have a greater torsion than τ_{max} because of the strongly varying vessel radius in patient datasets. Therefore, τ_{max} is multiplied by an empirically determined constant c, whose value is chosen by $c(r) = \frac{1}{2}(r-13)+3$.

Temporal Occurrence. During the cardiac cycle, vortices occur in the systole and/or the diastole. To determine the temporal occurrence, AVOCLA analyses the flow rate. The flow rate indicates how much milliliters of blood per second flow at a particular time in the cardiac cycle. Between systole and diastole there are significant changes in the flow rate that distinguishes between the two phases.

The diagram in Fig. 4(c) shows the flow rate of a proband for one heartbeat including the subsequent systole that is called flow curve. At the beginning of the systole, the flow rate increases due to the contraction of the heart, reaches its maximum after about 100 ms and drops thereafter. After about 246 ms a local minimum occurs (left, red point) that represents the systolic end and the diastolic beginning, respectively. During diastole, the flow rate is permanently low. With the renewed tightening of the heart muscle, the flow rate rises again (right, red point) and a new systole begins. AVOCLA identifies the phase end points to derive the percentage of systolic and diastolic path line points per vortex.

To determine the systolic end point, two basic flow curves are distinguished. If no negative flow rates are existent, the first local minimum is taken. However, flow curves of patients with valvular defects show often negative flow rates during diastole due to the defective closing of the AV. In such cases, the first local minimum belongs to the diastole, but the first zero crossing provides a reliable determination of the systolic end. For the diastolic end, the last occurring minimum is assumed, because afterwards the new systole starts and the flow rate increases again. To meet Req. 2, both points can be corrected by clicking into the diagram.

Vessel Section. The aorta is divided into four sections: the ascending aorta, aortic arch (ascending, descending), and descending aorta, see Fig. 4(d). For this, the centerline cusp point is determined that is approximately centrally located in the aortic arch and separates the ascending arch from the descending arch. Therefore, the discrete point representation of the centerline is used. In the underlying coordinate system the cusp point usually corresponds to the point with the smallest y-coordinate. Afterwards, the distance between the cusp point and the AV (first centerline point) is calculated. One third of this distance before and after the cusp point is declared as aortic arch. Sections previously and thereafter are defined as ascending and descending aorta.

Due to the large variation in occurring vessel shapes, the calculated cusp point or selected arch length may not correspond to the anatomical conditions. Thus, the user is able to correct the subdivision by changing the cusp point and/or the arch length (Req. 2). To derive the vortex associated aortic sections, we compute for each path line point the nearest centerline point using the Euclidean distance. In consultation with our experts, at least one third of the vortex path line points must be in a section so that this is taken into account.

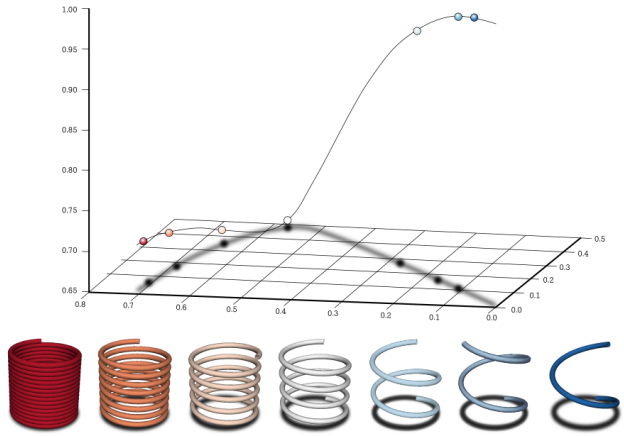

Figure 5: *The curve shows the eigenvalues of a helix depending on the turn number to determine the vortex shape. The colored helices correspond to the colored curve points.*

Vortex Size. From a clinical perspective, it is relevant if a vortex occupies on average less (minor) or more (pronounced) than 50 % of the vessel diameter, see Fig. 4(e) and 4(f), regardless of its temporal behavior. To determine the size, we calculate a 3D curve $C(u)$ per vortex that serves as a vortex centerline. For this, we use a *Least-Squares* spline approximation based on the path line points belonging to the vortex. The result of this approach is a piecewise polynomial function f of degree k, which consists of l polynomial sections. For our datasets, we observed that setting $l = 4$ is sufficient to capture the vortex centerline well. We also set $k = 4$, as higher values lead to higher amplitudes, because more outliers are considered and lower values could not capture the curved characteristics of the vortex well. For each dimension (x,y,z) of $C(u) = (f_1(u), f_2(u), f_3(u))^T$, a spline f_i is calculated. To identify f, we need function arguments and function values. Thus, we need an ordered set of points. For this, we use the largest extent of the vortex to sort the points along this axis. Therefore, we use an eigenvalue analysis to determine the largest eigenvalue λ_1 with its corresponding unit eigenvector e_1. Afterwards, every point p_i is projected along e_1: $d_i = \langle p_i, e_1 \rangle$. The ascending sorted distance values d_i serve as function arguments of f for all three dimensions (x,y,z). The amount of the function values forms the x, y and z-position of p_i belonging to d_i, respectively.

The resulting curve $C(u)$ is sampled at equidistant points $C(u_i) = c_i$ such that $\|c_i - c_{i+1}\| = 2mm$ holds. At each point c_i a local coordinate system is formed using the approach by Köhler et al. [KPG*16]. c_i is the center of this system and the local z-axis corresponds to the tangent at c_i. For each c_i, the nearest points p_i are determined based on the Euclidean distance that are projected in the xy-plane of c_i. Based on the projected points that are assumed

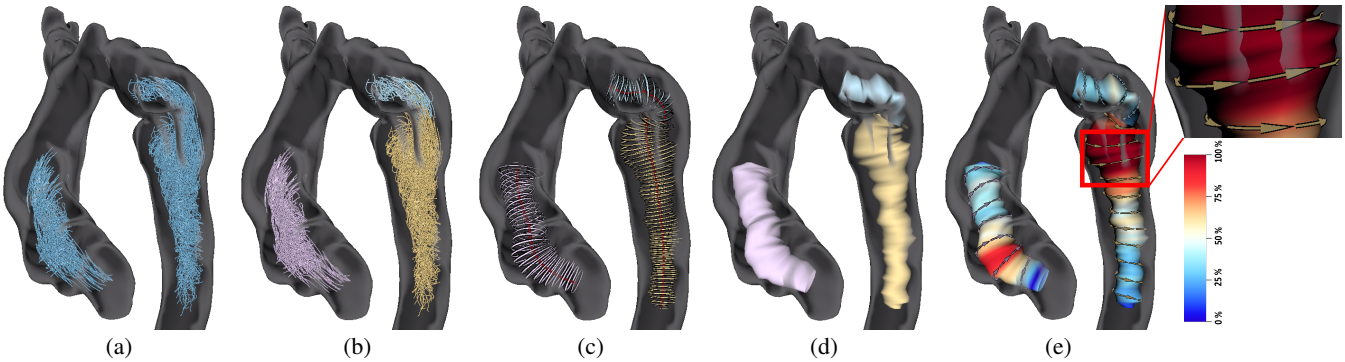

Figure 6: *3D glyph-based vortex visualization. The vortex-representing path lines (a) are clustered (b). For each cluster, a cubic spline (red) is calculated, and at each spline point an ellipse approximates the local vortex expansion (c). The ellipses are triangulated to a surface (d) on which the percentage size and RD are depicted using a color-coding and arrow glyphs (e).*

to be normally distributed, a confidence ellipse is calculated with a confidence interval of 95 %. The remaining 5 % are declared as outliers and are not considered for the determination of the vortex size.

However, the number of projected points can vary greatly. Therefore, an ellipse is only calculated if the number of projected points exceeds a threshold that is set to the 5 % quantile of the projected points at every c_i. Afterwards, the area of the confidence ellipse at c_i is compared to the area of the vessel cross-section at the centerline point closest to c_i. The area of the vessel cross-section can be derived from the known vessel radius at the centerline point. In this way, it can be determined how much of the vessel cross-section the vortex percentage takes up at c_i. Finally, the average size is calculated for all c_i, which basically allows a more detailed size division than the binary expert classification (Req. 3).

Rotation Direction. The RD is divided into right- and left-handed, see Fig. 4(g) and 4(h). If the vortex rotates in flow direction clockwise around the centerline, it is classified as right-handed, otherwise as left-handed. The RD is determined for each path line segment that consists of two successive points p_i and p_{i+1}. Both points are projected in the xy-plane of the point $c(p_i)$ that is the nearest centerline point of p_i. The calculation of $c(p_i)$ and its local coordinate system was explained in the previous section.

For the projected points p'_i and p'_{i+1}, we identify the angle to the x-axis of the plane using the arc tangent function with two arguments. The signed angle sizes indicate in which quadrant of the plane p'_i and p'_{i+1} are located. For example, if p'_i and p'_{i+1} are located in the first and second quadrant, they present a right-handed segment. If p'_i is arranged in the fourth and p'_{i+1} in the third quadrant, a left-handed segment exists. If they are located in diagonal quadrants, the intersection between the connecting line and the y-axis is used to define a RD. Depending on whether a path line has more right or left rotating segments, it is classified as right- or left-handed. Similarly, the vortex RD depends on the amount of right- and left-handed path lines. This enables a percentage of right- and left-handed flow per vortex, which extends the binary division (Req. 3).

5.3. Vortex Visualization

To facilitate the examination and interpretation of the classification results, we developed a 2D and 3D representation that convey the calculated vortex characteristics (Req. 4). In the following, both visualizations are explained in detail.

5.3.1. 2D Vortex Plot

For an occlusion-free depiction of the complex spatio-temporal vortex behavior we extended the 2D plot by Köhler et al. [KMP*15], see Fig. 1. The temporal component of each path line point is mapped to the angle. Therefore, the plot area is divided into T equal large sectors, where T is the number of measured time steps. Thus, a clock metaphor is used, where the first time step is located at 12 o'clock; the direction is clockwise. Red time points represent the systolic phase and blue time points show the diastole. Moreover, each sector of the plot is subdivided into four segments along the radius r that represent the four aortic sections. The spatial position starts at $r = \sqrt{0.1}$, which represents the AV location. For each path line point, the nearest centerline point is calculated. Depending on the corresponding vessel section, the radius is linearly interpolated from the known radii of the centerline points that separate the individual aortic sections. Thus, increasing r encodes positions in the aortic arch and descending aorta. The square root is used to ensure that inner and outer parts of the plot are represented with equally large areas. Finally, each plot segment is colored according to the cluster portions. However, the segments are only colored if at least one third of the vortex path line points lie in the associated aortic sections. Furthermore, diastolic path lines, which account for less than 10 % of the total flow, were not considered as diastolic vortex flow by our medical expert. Thus, the associated plot segments are not colored.

5.3.2. 3D Glyph-based Visualization

We developed a 3D vortex visualization to convey the radial expansion and RD of vortices. Therefore, we determined the surface that envelops the vortex, whereupon both properties are mapped. For the determination of the enveloping surface, the confidence ellipses at the spline points of C_u are used. Each ellipse is sampled

at equidistant points and the positions are transformed back in the 3D coordinate system of C_u. Fig. 6(c) shows the calculated splines and associated ellipses for three clusters. The 3D points of two adjacent ellipses are triangulated, see Fig. 6(d). It may happen that no ellipse was calculated for a spline point. In such cases, missing ellipses were linearly interpolated from adjacent ellipses. The radial expansion is visualized using a linear color scale, see Fig. 6(e). Areas that occupy less than 50 % of the vessel cross-section are mapped to a bluish color and otherwise to a reddish color. The RD is depicted by arrows on a quadstrip around the surface, using the approach by Lawonn et al. [LGV*15]. For a right-handed vortex, the arrows point in flow direction to the upper right, otherwise to the top left. Furthermore, the arrows receive the associated cluster color to generate a correlation between the 2D and 3D depiction.

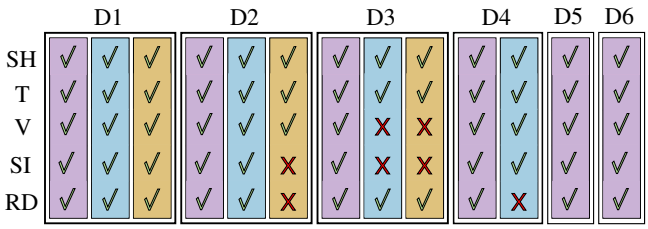

Figure 7: *Classification results for six datasets according to: shape (SH), temporal occurrence (T), vessel section (V), size (SI) and rotation direction (RD). Each colored column represents a vortex. The marks show matches and mismatches between the ground truth and AVOCLA's results.*

6. Evaluation

We performed a qualitative evaluation of AVOCLA's results against a manually generated ground truth of our collaborating experts. We used 15 datasets: 2 healthy volunteers with a slight physiologic helix in the aortic arch during systole and 13 patients with different CVDs. Each patient has prominent vortex flow in different parts of the aorta. The clustering differentiates at most ten clusters via color. More is not necessary because no more than four vortices occur in our datasets. The remaining six clusters are used to depict laminar flow or noise that can be excluded from the subsequent classification. Moreover, the experts can merge clusters or change the cluster number if the automatically calculated number is not appropriate. For the classification, the experts can manually correct the aortic subdivision by shifting the cusp point or changing the arc length. In addition, systolic and diastolic end points can be adapted manually by clicking into the flow rate diagram, see Fig. 4(c).

6.1. Ground Truth

The ground truth, which comprises the number of vortex clusters and their characteristics, was manually generated by our experts using standard flow visualization techniques, such as illumination and animation. The vessel surface is depicted using the ghosted view approach [GNKP10]. Processing the 15 datasets took 3h. Especially the determination of the vortex size has been described as very difficult. The experts have to view the vortices from many perspectives.

6.2. User Study

We conducted a user study with 12 probands, one physician and 11 researchers with background in medical visualization, where our vortex visualizations were compared to a standard 3D path line depiction embedded in the vessel surface. Thereby, the vessel sections are color-coded on the centerline similar to Fig. 4(d). The goal was to assess the capabilities of our 2D and 3D visualization for expressing AVOCLA's results. The subjects were asked to perform four tasks:

1. Assessment of the vortex belonging vessel sections.
2. Determination of the vortex belonging cardiac phase.
3. Identification of the vortex rotation direction.
4. Estimation of the minor or pronounced vortex size.

For each task, we chose four datasets. Two are visualized by our approach (2D plot: task 1 and 2, 3D glyph: task 3 and 4) and two with the standard path line view (PV). The subjects were divided into two groups, and both groups received the same datasets. However, group A started each task using the PV and group B always begun with our technique. Moreover, cases that were shown to group A in the PV, were processed by group B using the respective own approach and vice versa. Changing the techniques should reduce the influence of learning effects. The exchange of datasets between groups ensures that each vortex was evaluated using both techniques. The results are compared to the ground truth. During the evaluation, we noted the subjects' spoken comments and they had to answer a short questionnaire using a five-point Likert scale ($--$, $-$, $\circ$, $+$, $++$):

1. How difficult was it to solve the task based on the particular visualization method?
2. How certain are you with your assessment?

7. Results and Discussion

This section presents the results of AVOCLA compared to the ground truth and the user study. Moreover, we discuss current limitations of AVOCLA. Our approach is implemented on an Intel Core i7 CPU with 2 GHz, 12 GB RAM and an NVidia GeForce GT540M. The computation time per case is between 12 and 20 s, depending on the amount of path lines. This includes all steps of the pipeline shown in Fig. 3. The used agglomerative hierarchical clustering [MLK*16] could cluster all datasets correctly according to the manual expert clustering (Req. 1 fulfilled).

7.1. Classification Results

The 15 used datasets contain a total of 30 vortices. Fig. 7 presents exemplarily AVOCLA's results for six datasets and the corresponding clustering as well as the 2D and 3D depiction in Fig. 8. In the following, the colored vortices from these images are referenced.

Vortex Shape: AVOCLA determined the shape correctly for all vortices. Five vortices were manually classified as vortex, e.g., the blue vortex of D1. These vortices contain at least 62 % vortical and

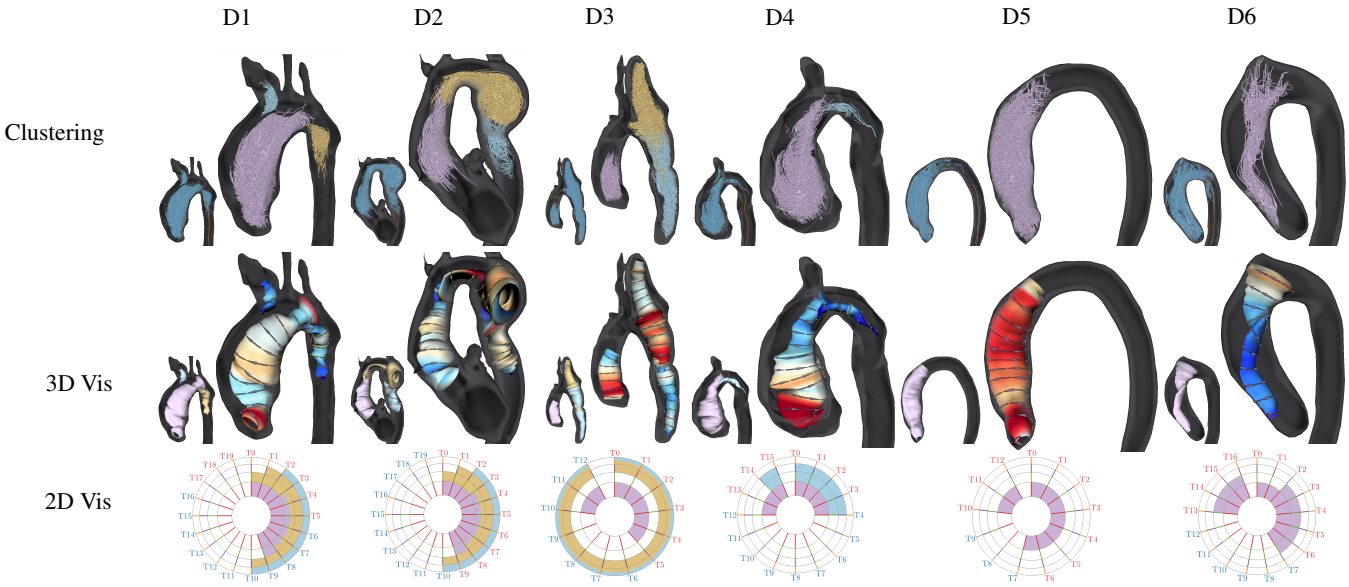

Figure 8: *Clustering and visualization of the classification results for the six datasets from Fig. 7.*

at most 38 % helical flow. Four vortices were manually classified as helix, e.g., the purple vortex of D6. AVOCLA computed for these a minimum helical component of 64.6 % and at most 35.4 % vortical flow. The remaining vortices were manually classified as intermediate shapes, e.g., the purple vortex of D2. The calculations show very similar flow components with at least 41.8 % helical and 54.6 % vortical flow.

Temporal Occurrence: For the classification of the temporal occurrence, AVOCLA initially identifies the systolic and diastolic endpoint. These points could be automatically calculated correctly for all datasets. Based on this, AVOCLA determined the correct phase for all vortices. Systolic vortices contain at least 90.7 % systolic and maximum 9.3 % diastolic flow. Vortices in both phases exhibit more similar flow components with a maximum of 68 % systolic and a minimum of 32 % diastolic flow.

Vessel Section: AVOCLA divides the aorta automatically into four sections. This partition correlated in 10 datasets with the manual subdivision, whereas five cases had to be manually corrected, e.g., D3. The coarctation of the aortic arch led to a strong vessel deformation, so that the automatic division failed. The subsequent determination of the vascular sections conformed with the ground truth for all vortices.

Vortex Size: Eight vortices are manually classified as minor and the calculated sizes are in the range of 16.8 % - 37.1 %, which reflects the ground truth. However, for one vortex with a size of 37.1 % the experts expected a smaller size. In this case, the assumed normal distribution of the path line points is not satisfied, whereby AVOCLA overestimates the size. This can also cause that the glyph drops out of the vessel surface (D2: brown). For six vortices, the experts were uncertain in their size classification. They supposed that their expansion is close to the 50 % limit. Three of them were classified as slightly smaller (rather minor) and three as slightly larger (rather pronounced). The rather minor vortices have a calculated size of 46.9 % - 48.3 %, whereas the size of the rather pronounced vortices is between 50.9 % and 53.6 %. All remaining vortices are manually classified as pronounced, that is correctly determined by AVOCLA with a calculated size greater than 50 %. But for three vortices AVOCLA underestimated the vortex size (D2: brown and D3: blue and brown). In these cases, the 95 % quantile caused that too many path line points are excluded from the ellipse calculations, because compared to other datasets far fewer outliers are existent.

Rotation Direction: Concerning the RD, AVOCLA calculated a correct result for 28 vortices. Two vortices (D3: brown and D4: blue) run neither right- nor left-handed after manual assessment. Instead, the path lines run orthogonal to the centerline. We called this rotation *roll over rotation*, which cannot be detected by AVOCLA until now.

7.2. Results of the User Study

For the interpretation of our predefined Likert score categories, we provide the number P of participants who chose the individual categories.

Task 1 Vessel Sections: Each subject had to assess the vessel sections for eight vortices, four with the 2D plot and four with the PV. Thereby, the first vortex (V1) is located in one section and the other three (V2-V4) are located in more sections. For both techniques, all probands determined the correct section for V1. For V2-V4, a total of 36 (12 probands·3 vortices) assessments per technique are given. Using the PV, the correct sections are given 28 times, whereas in eight cases additional sections are determined. For the 2D plot the correct sections were identified in all cases. Moreover,

all subjects perceived the plot as very simple ($P(++) = 12$) and certain ($P(++) = 9$; $P(+) = 3$). The simplicity of the PV was rated with ($P(++) = 3$; $P(+) = 7$; $P(o) = 2$), whereas its certainty was rated with ($P(++) = 8$; $P(+) = 3$; $P(\circ) = 1$). To see the aortic sections on the centerline, the participants had to deselect clusters, which complicates the task. Furthermore, they describe the estimation of the percentage of each section to be difficult, which leads to a reduced certainty.

Task 2 Cardiac Phase: Each proband had to assess the cardiac phase for six vortices, three per technique. The first vortex (V1) occurs in the systole, whereas the other two (V2-V3) are extended to both phases. For both techniques, all participants classified V1 correctly as a systolic vortex. V2 and V3 were also correctly classified by all probands using the 2D plot, whereas 2 participants described V2 as a systolic vortex based on the PV. Similar to the first task, the simplicity of the plot was rated with $P(++) = 11$ and $P(+) = 1$, because the vessel sections and phases can be read out without any interaction. Its certainty was stated with $P(++) = 7$, $P(+) = 3$ and $P(\circ) = 2$, and the subjects pointed out that the plot opposite the PV required a higher confidence by the user as to the accuracy of the colored cells. The simplicity of the PV was rated with $P(++) = 3$, $P(+) = 7$, $P(\circ) = 1$ and $P(-) = 1$ because of the necessary cluster deselection to observe spatio-temporal vortices individually. Uncertainties based on the PV formed when individual lines were present in the diastole ($P(++) = 4$; $P(+) = 7$; $P(\circ) = 1$).

Task 3 Rotation Direction: To determine the RD, six vortices were selected, three per technique (V1-V3). V1 was located in the ascending branch and more than 90 % of the lines had the same RD. V2 had a more difficult distribution of the RD from about 70 % to 30 % and V3 was located in the poorly visible descending aorta. For both techniques, all subjects determined the correct RD for V1. Using the 3D glyph, the RD was also correctly determined for V2 and V3 by all probands. Based on the PV, 11 of the 18 given assessments for V2 and V3 were correct, and 7 times a wrong RD was specified. The reliable results using the 3D glyph are also reflected in the perceived simplicity ($P(++) = 9$; $P(+) = 3$) and certainty ($P(++) = 11$; $P(+) = 1$). In comparison, the simplicity of the PV is rated with $P(+) = 1$, $P(\circ) = 4$, $P(-) = 5$ and $P(--) = 2$. The certainty is also reduced ($P(+) = 4$; $P(\circ) = 4$; $P(-) = 4$). The glyph abstracts the partially complex flow data and is therefore more appropriate to depict the RD, especially for the difficult V2 and V3. Using the PV, the detection of the correct RD is highly dependent on the complexity and location of the vortex.

Task 4 Vortex Size: The vortex size has to be determined for three vortices per technique, V1 was considerably minor or pronounced (< 40 % or > 60 %) and V2 and V3 are classified as rather minor or pronounced (> 40 % and < 60 %) by the experts. By using the 3D glyph, all probands could correctly classify considerably minor or pronounced vortices. Based on the PV, 3 of 18 given assessments for V1 were wrong. One rather pronounced vortex was wrongly classified by one proband using the 3D glyph, whereas for the PV 7 of the 18 given assessments for V2 and V3 were not correct. The subjects describe the size estimation based on the PV as difficult ($P(+) = 1$; $P(\circ) = 3$; $P(-) = 6$; $P(--) = 2$), because a high interaction effort was needed to see the vortex of all sides. Furthermore, they were unsure with the estimation of the distance between the vortex and the vessel wall, which is why the certainty was rated with $P(\circ) = 5$, $P(-) = 6$ and $P(--) = 1$. The color-coded 3D glyph facilitates the estimation of the vortex size, which is reflected in the improved simplicity ($P(++) = 3$; $P(+) = 7$; $P(\circ) = 2$). In addition, the certainty of the volunteers has risen in terms of their estimates ($P(++) = 2$; $P(+) = 4$; $P(\circ) = 5$; $P(-) = 1$).

8. Conclusion and Future Work

In this paper, we presented the method AVOCLA for a semi-automatic classification of aortic vortex flow extracted from 4D PC-MRI data. Each vortex is classified according to specific characteristics that are calculated based on geometrical properties and relations of the path lines and the vessel surface. This assures a comparability of the results. In contrast, manual classifications are time-consuming and not standardized. The vortex classification requires a reliable clustering of the incoming path lines. We choose the agglomerative hierarchical approach by Meuschke et al. [MLK*16] that is robust against noise and able to separate spatio-temporally adjacent vortices. Based on the requirements derived from consultations with our medical expert and a literature analysis, we identify five important vortex properties for the classification: shape, temporal occurrence, vessel section, size, and RD. A common advantage of the clustering and classification is the possibility to incorporate expert knowledge. The cluster number can be changed and clusters can be merged or deselected from the following classification. Moreover, AVOCLA's results, such as the determination of the vessel sections, can be manually corrected. By manually editing, the expert is allowed to deal with various aortic shapes caused by different CVDs. Furthermore, our results are able to extend the binary expert classifications such as the vortex shape.

A 2D and 3D visualization present the calculated vortex properties. The 2D depiction in form of a circular plot shows the spatio-temporal vortex behavior without any occlusions. The 3D representation displays the size as well as the RD by using a color-coding and arrow glyphs. The vortex shape is currently only indirectly depicted by the extent of the 3D glyph. But a reliable examination of intermediate shapes is not guaranteed, which should be improved in the future by adapting the slope of the used quad strip around the glyph surface to the percentage helical flow. Moreover, the calculation of the vortex size should be further enhanced. Possible under- or overestimations could be reduced by using optimization methods for the ellipse calculations. A better ellipse approximation would also avoid that the glyph surface drops out of the vessel surface. In addition, the wall motion should be considered, since the vortex size is changing relative to the expansion or contraction of the vessel wall. Furthermore, other experts should be included in the evaluation of AVOCLA's results and we have to check the extent to which a more detailed subdivision of the size or RD improves the binary classification from a medical point of view.

Acknowledgements

This work was partially funded by the BMBF (STIMULATE:13GW0095A). The authors like to thank the Heart Center Leipzig for providing us the datasets.

References

[BMGS13] BORN S., MARKL M., GUTBERLET M., SCHEUERMANN G.: Illustrative Visualization of Cardiac and Aortic Blood Flow from 4D MRI Data. In *IEEE Pacific Vis* (2013), pp. 129–36. 2

[BPM*13] BORN S., PFEIFLE M., MARKL M., GUTBERLET M., SCHEUERMANN G.: Visual Analysis of Cardiac 4D MRI Blood Flow Using Line Predicates. *IEEE Trans Vis Comput Graph 19* (2013), 900–12. 2

[DBB*15] DYVERFELDT P., BISSELL M., BARKER A. J., BOLGER A. F., ET AL.: 4D Flow Cardiovascular Magnetic Resonance Consensus Statement. *J Cardiovasc Magn Reson 17*, 1 (2015), 72. 1

[FHJ*07] FRYDRYCHOWICZ A., HARLOFF A., JUNG B., ZAITSEV M., WEIGANG E., BLEY T. A., LANGER M., HENNIG J., MARKL M.: Time-resolved, 3-Dimensional Magnetic Resonance Flow Analysis at 3 T: Visualization of Normal and Pathological Aortic Vascular Hemodynamics. *Computer Assisted Tomography 31*, 9 (2007), 9–15. 3

[FMH*11] FRYDRYCHOWICZ A., MARKL M., HIRTLER D., HARLOFF A., SCHLENSAK C., GEIGER J., STILLER B., ARNOLD R.: Aortic Hemodynamics in Patients With and Without Repair of Aortic Coarctation: In Vivo Analysis by 4D Flow-Sensitive Magnetic Resonance Imaging. *Invest Radiol 46*, 5 (2011), 317–25. 2, 3

[FSS*12] FRANÇOIS C., SRINIVASAN S., SCHIEBLER M., REEDER S., NIESPODZANY E., LANDGRAF B., WIEBEN O., FRYDRYCHOWICZ A.: 4D Cardiovascular Magnetic Resonance Velocity Mapping of Alterations of Right Heart Flow Patterns and Main Pulmonary Artery Hemodynamics in Tetralogy of Fallot. *J Cardiovasc Magn Reson 14*, 1 (2012), 16. 3

[GLvP*12] GASTEIGER R., LEHMANN D. J., VAN PELT R., JANIGA G., BEUING O., VILANOVA A., THEISEL H., PREIM B.: Automatic Detection and Visualization of Qualitative Hemodynamic Characteristics in Cerebral Aneurysms. *IEEE Trans Vis Comput Graph 18(12)*, 12 (2012), 2178–87. 2

[GMH*12] GEIGER J., MARKL M., HERZER L., HIRTLER D., LOEFFELBEIN F., STILLER B., LANGER M., ARNOLD R.: Aortic Flow Patterns in Patients with Marfan Syndrome assessed by Flow-Sensitive Four-Dimensional MRI. *J Magn Reson Imaging 35*, 3 (2012), 594–600. 3

[GNKP10] GASTEIGER R., NEUGEBAUER M., KUBISCH C., PREIM B.: Adapted Surface Visualization of Cerebral Aneurysms with Embedded Blood Flow Information. In *Proc: EG Vis Comput Biol Med* (2010), pp. 25–32. 2, 7

[HEWK03] HEIBERG E., EBBERS T., WIGSTRÖM L., KARLSSON M.: Three-Dimensional Flow Characterization using Vector Pattern Matching. *IEEE Trans Vis Comput Graph 9*, 3 (2003), 313–9. 2

[HHM*10] HOPE M. D., HOPE T. A., MEADOWS A. K., ORDOVAS K. G., URBANIA T. H., ALLEY M. T., HIGGINS C. B.: Bicuspid Aortic Valve: Four-Dimensional MR Evaluation of Ascending Aortic Systolic Flow Patterns. *Radiology 255*, 1 (2010), 53–61. 1, 2, 3

[HMW*07] HOPE T. A., MARKL M., WIGSTRÖM L., ALLEY M. T., MILLER D., HERFKENS R.: Comparison of Flow Patterns in Ascending Aortic Aneurysms and Volunteers using Four-Dimensional Magnetic Resonance Velocity Mapping. *J Magn Reson Imaging 26*, 6 (2007), 1471–9. 3

[HWS*12] HOPE M. D., WRENN J., SIGOVAN M., FOSTER E., TSENG E. E., SALONER D.: Imaging Biomarkers of Aortic Disease - Increased Growth Rates with Eccentric Systolic Flow. *J Amer Coll Cardiol 60* (2012), 356–7. 1, 2

[KBV*16] KÖHLER B., BORN S., VAN PELT R. F. P., HENNEMUTH A., PREIM U., PREIM B.: A Survey of Cardiac 4D PC-MRI Data Processing. *Computer Graphics Forum* (2016), to appear. 2

[KGP*13] KÖHLER B., GASTEIGER R., PREIM U., THEISEL H., GUTBERLET M., PREIM B.: Semi-automatic Vortex Extraction in 4D PC-MRI Cardiac Blood Flow Data using Line Predicates. *IEEE Trans Vis Comput Graph 19*, 12 (2013), 2773–82. 1, 2, 3

[KMP*15] KÖHLER B., MEUSCHKE M., PREIM U., FISCHBACH K., GUTBERLET M., PREIM B.: Two-Dimensional Plot Visualization of Aortic Vortex Flow in Cardiac 4D PC-MRI Data. In *Proc: Bildverarb Med* (2015), pp. 257–61. 2, 6

[KPG*16] KÖHLER B., PREIM U., GROTHOFF M., GUTBERLET M., FISCHBACH K., PREIM B.: Robust Cardiac Function Assessment in 4D PC-MRI Data of the Aorta and Pulmonary Artery. *Comput Graph Forum 35*, 1 (2016), 32–43. 5

[KYM*93] KILNER P., YANG G., MOHIADDIN R., FIRMIN D. N., LONGMORE D. B.: Helical and Retrograde Secondary Flow Patterns in the Aortic Arch Studied by Three Directional Magnetic Resonance Velocity Mapping. *Circulation 88* (1993), 2235–47. 3

[LGP14] LAWONN K., GASTEIGER R., PREIM B.: Adaptive Surface Visualization of Vessels with Animated Blood Flow. *Comput Graph Forum 33(8)* (2014), 16–27. 2

[LGV*15] LAWONN K., GLASSER S., VILANOVA A., PREIM B., ISENBERG T.: Occlusion-free Blood Flow Animation with Wall Thickness Visualization. *IEEE Trans Vis Comput Graph 22(1)*, 1 (2015), 728–37. 7

[MBS*15] MAHADEVIA R., BARKER A. J., SCHNELL S., ENTEZARI P., KANSAL P., FEDAK P. W. M., MALAISRIE S. C., MCCARTHY P., COLLINS J., CARR J., MARKL M.: Bicuspid Aortic Cusp Fusion Morphology Alters Aortic 3D Outflow Patterns, Wall Shear Stress and Expression of Aortopathy. *Circulation 129*, 6 (2015), 673–82. 1, 3

[MGH*11] MARKL M., GEIGER J., HERZER L., STILLER B., ARNOLD R.: 3D Aortic Blood Flow in Patients with Marfan Syndrome: Changes in Hemodynamics and Correlation with Aortic Geometry. *International Society for Magnetic Resonance in Medicine 19* (2011), 725. 3

[MLK*16] MEUSCHKE M., LAWONN K., KÖHLER B., PREIM U., PREIM B.: Clustering of Aortic Vortex Flow in Cardiac 4D PC-MRI Data. In *Proc: Bildverarb Med* (2016), pp. 182–87. 4, 7, 9

[OLK*14] OELTZE S., LEHMANN D. J., KUHN A., JANIGA G., THEISEL H., PREIM B.: Blood Flow Clustering and Applications in Virtual Stenting of Intracranial Aneurysms. *IEEE Trans Vis Comput Graph 20(5)* (2014), 686–701. 2

[PB13] PREIM B., BOTHA C.: *Visual Computing for Medicine*, 2 ed. Morgan Kaufmann, 2013. 2

[PVS*09] PICCINELLI M., VENEZIANI A., STEINMAN D. A., REMUZZI A., ANTIGA L.: A Framework for Geometric Analysis of Vascular Structures: Application to Cerebral Aneurysms. *Trans Med Imag 28*, 8 (2009), 1141–55. 3

[SS06] SALZBRUNN T., SCHEUERMANN G.: Streamline Predicates. *IEEE Trans Vis Comput Graph 12*, 6 (2006), 1601–12. 2

[vPBB*10] VAN PELT R., BESCÓS J. O., BREEUWER M., CLOUGH R. E., GRÖLLER M. E., TER HAAR ROMENY B., VILANOVA A.: Exploration of 4D MRI Blood Flow using Stylistic Visualization. *IEEE Trans Vis Comput Graph 10*, 6 (2010), 1339–47. 2

[vPFCV14] VAN PELT R., FUSTER A., CLAASSEN G., VILANOVA A.: Characterization of Blood-Flow Patterns from Phase-Contrast MRI Velocity Fields. In *EuroVis - Short Papers* (2014). 2

[vPJtHRV12] VAN PELT R., JACOBS S., TER HAAR ROMENY B., VILANOVA A.: Visualization of 4D Blood-Flow Fields by Spatiotemporal Hierarchical Clustering. *Comput Graph Forum 31*, 3pt2 (2012), 1065–74. 2

[VPvP*14] VILANOVA A., PREIM B., VAN PELT R., GASTEIGER R., NEUGEBAUER M., WISCHGOLL T.: Visual Exploration of Simulated and Measured Blood Flow. In *Scientific Visualization*. Springer London, 2014, pp. 305–24. 2

[vSCG*15] VON SPICZAK J., CRELIER G., GIESE D., KOZERKE S., MAINTZ D., BUNCK A. C.: Quantitative Analysis of Vortical Blood Flow in the Thoracic Aorta Using 4D Phase Contrast MRI. *PLoS ONE 10*, 9 (2015). 2